International Journal of Heat and Mass Transfer 149 (2020) 119203

Contents lists available at ScienceDirect

International Journal of Heat and Mass Transfer

journal homepage: www.elsevier.com/locate/hmt

Experimental and numerical study on convective boiling in a staggered array of micro pin-fin microgap

Liang-Han Chien[a,b], Yi-Ting Cheng[a,b], Ying-Liang Lai[a,b], Wei-Mon Yan[a,b,*], Mohammad Ghalambaz[c,d,**]

[a] Department of Energy and Refrigerating Air-Conditioning Engineering, National Taipei University of Technology, Taipei 10608, Taiwan
[b] Research Center of Energy Conservation for New Generation of Residential, Commercial, and Industrial Sectors, National Taipei University of Technology, Taipei 10608, Taiwan
[c] Department for Management of Science and Technology Development, Ton Duc Thang University, Ho Chi Minh City, Vietnam
[d] Faculty of Applied Sciences, Ton Duc Thang University, Ho Chi Minh City, Vietnam

ARTICLE INFO

Article history:
Received 14 September 2019
Revised 21 November 2019
Accepted 9 December 2019
Available online 14 December 2019

Keywords:
Micro-pin-fin
Staggered array
Microgap
FC-72
Columnar nucleation pin-fin
Nucleate boiling heat transfer

ABSTRACT

The flow patterns, heat transfer and pressure drop of convective boiling of dielectric fluid, FC-72, in a micro-gap are investigated experimentally. The surface of the microgap is enhanced with a staggered array of micro pin-fins. The enhanced surface of the microgap with the size of 10 × 10 mm^2 is subject to an electrical heat source. The micro-pin-fins are etched as cubic columns of 100 μm size and arranged in a staggered arrangement with 400 μm pitch in both transverse and longitudinal directions. The inside of the micro pin-fins is nucleated with a cavity of cylindrical shape with diameter of 60 μm and an opening with a size of either 15 μm or 45 μm width. The opening of the cavities of the micro-pin-fins is aligned toward the down-stream. For the case of single-phase flow, a numerical analysis is performed, and the pressure drop and velocity fields are investigated in the micro-gap. The experiments were performed for various mass fluxes ranging from 94 to 275 kg/m^2s and heat flux ranging from 0 to 10 W/cm^2, and at two saturation temperatures of 35 and 50 °C. For the case of single-phase heat transfer, the experimental results are compared with the pin-fins having 45 μm cavity opening and found that the effect of cavity opening is significant when the mass flux is high. The surface-superheat at the onset of boiling is reduced by reducing the cavity opening-width from 45 to 15 μm. The microgap having nucleation cavity with cavity opening-width of 15 μm results in a 3.44 °C smaller surface-superheat than that of 45 μm opening-width. The convective heat transfer coefficient increases with the increase of mass flux, regardless of the flow type. Moreover, the variation of the pin-fin opening-widths does not influence the convection heat transfer rate. For single-phase flow, the heat flux shows a negligible effect on pressure drop, and the pressure drop increases with increasing mass flux. For two-phase flow, the pressure drop increases drastically with increasing heat flux. A smaller cavity opening-width results in a smaller pressure drop when the mass flux is high. The flow observation shows two distinct flow patterns in the microgap at the beginning of the bubble nucleation.

1. Introduction

The micro-scale flow boiling in microchannels and microgaps has been subject of various recent studies and has attracted the attention of many researchers. The flow boiling in microstructures is of growing interest due to a relatively high heat transfer coefficient, steady saturation temperature, and low pumping power, compared to a single-phase flow [1]. The onset of boiling heat transfer increases the convective heat transfer coefficient significantly and is the desired phenome in forced convection boiling. However, in practice, some degrees of superheat may be occurred, which delays the onset of boiling heat transfer to large temperature differences. In such situations, the flow remains single-phase with low convective heat transfer capability and result in overheating of the system. The single-phase flow in microchannels and microgap is of interest as it occurs before the onset of boiling flow heat transfer. Considering single-phase heat transfer, Kosar and Peles [2] used microelectromechanical process technology to etch a microchannel heatsink with a depth of 147 μm on a germanium

* Corresponding author at: Department of Energy and Refrigerating Air-Conditioning Engineering, National Taipei University of Technology, Taipei 10608, Taiwan.
** Corresponding author at: Ton Duc Thang University, Ho Chi Minh City, Vietnam.
E-mail addresses: wmyan@ntut.edu.tw (W.-M. Yan), mohammad.ghalambaz@tdtu.edu.vn (M. Ghalambaz).

https://doi.org/10.1016/j.ijheatmasstransfer.2019.119203
0017-9310/

wafer. Five different fin shape surfaces, including circle shape, rectangle shape, hydrofoil shape, and droplet shape along with parallel or staggered arrays were etched, and the heat transfer performance was tested for water as the working fluid. In these cases, heat transfer performance and pressure loss are compared for Reynolds number in the range of 14~720. The outcomes demonstrate that the surface of the hydrofoil shaped fin can enhance the heat transfer performance in the middle Reynolds number range.

Wang et al. [3] investigated the single-phase heat transfer over a single pin-fin in a microchannel both experimentally and numerically. They characterized three flows, namely laminar flow with steady wake, laminar flow with unsteady wake, and turbulent flow depending on the Reynolds number. They used an array of micro resistance temperature detectors to capture the local temperature of the microchannel surface with a high resolution. The authors reported the improvement of the local heat transfer coefficient at the trailing edge of a wake region at downstream flow. Kong et al. [4] examined the thermal and hydraulic performance of a staggered array of micro pin-fins with R245fa as the working fluid. Authors tested three different samples of micro pin-fin arrays including 31 $\times$ 131 rows of 45–100 μm diameter cylindrical micro-pin-fins with a height about 200 μm and center-to-center pin spacings of 74–298 μm. The results show that the heat transfer coefficient is a function of pin spacing and mass flow rate and the average heat transfer coefficient was up to 18.2 kW/(m^{2}K). These authors utilized ANSYS Fluent for their numerical calculations. Absolute errors of 9.1% and 14.3% were found between the numerical results and experimental results for the heat transfer and the pressure drop, respectively. Xiangfei et al. [5] theoretically investigated the single-phase heat transfer in a microgap enhanced with an array of nucleated Piranha micro pin-fins. Although the micro-pin-fins can enhance the heat transfer in a microgap or microchannel, their convective heat transfer coefficient is limited. Hence, the flow boiling heat transfer is essential for further enhancement of heat transfer. In this regard, many researchers tried to furthered improve the flow boiling in various types of microchannels such as using auxiliary channels [6], multiple micro-nozzles [7], high surface microchannel [8], zigzag microchannel [9], surface treatment (super-hydrophilic silicon wafer) [10], or using nanofluids [11]. Huh and Kim [12] studied the pressure drop of a boiling heat transfer of water in a single microchannel. Hsieh and Lin [13] investigated the subcooled boiling flow and heat transfer of water in a rectangular channel with triangular cavities on sidewalls.

There are also several attempts to improve the boiling heat transfer in microgaps by using rectangular fins [14], staggered circular cylindrical pin-fins [15], or a combination of pin-fins and interconnected reentrant microchannels [16]. Lie et al. [17] addressed the boiling heat transfer of FC-72 in a microgap with a pin-fin enhanced surface. Kuo and Peles [18] used a tantalum wafer as the substrate to etch five smooth surfaces on the top. The length of the channel was 10,000 μm, while the channels' height and width were 200 μm, and 250 μm, respectively. 50 μm cylindrical cavities with 200 μm spacing were etched at both sides of the channel's walls. Each cylindrical cavity is etched with an opening pore of 7.5 μm width. Kuo and Peles utilized HFE-7000 as the working fluid and investigated the flow and heat transfer in the channel. The experimental results show that the presence of wall cavities improves the convective heat transfer coefficient and reduces the superheat temperature. Kosar and Peles [19] utilized a staggered array of hydrofoil-shape pin-fins to enhance the boiling heat transfer of R-123 in a microgap. They performed the experiments for mass fluxes from 976 to 2349 kg/m^{2}s an effective heat fluxes ranging from 19 to 312 W/cm^2. They found that the heat transfer coefficient grows by the raise of heat flux until it reaches to a maximum value, and then it monotonically drops until it reaches to the critical heat flux condition. The flow maps were investigated and bubbly, wavy intermittent, and spray-annular flow patterns were noticed, depending on the working fluid mass flux and the surface heat flux.

Krishnamurthy and Peles [20] addressed boiling heat transfer of water in a microgap enhanced with a staggered array of circular micro-pin-fins. Other pin-fin configurations such as a parallel array of circular [21], square [22, 23] micro pin-fins, and a staggered array of square [22, 24], circular [24], diamond [24], streamline [24], and Piranha [1] micro pin-fins, for boiling flow were tested. The effect of a straight-finned and oblique-finned microgap is also addressed [25]. The idea of nucleation of channel walls is investigated in the early study of Kuo and Peles [18] for microchannels. Later Woodcock et al. [1, 26], Yu et al. [27, 28] utilized nucleated Piranha pin-fins to reduce superheating and improve heat transfer. The nucleation of pin-fins reduces the single-phase flow heat transfer compared to plane pin-fins due to the reduction of fin heat transfer. However, the nucleation cavities provide low-pressure pores and facilitate bubble formation. Very recently, Liao et al. [29], and Chien et al. [30, 31] examined the effect of nucleation of square pin-fins in a parallel array. The pin-fins were columnar squares of size 100 μm, in which the center of each pin-fins nucleated by a cylindrical cavity of diameter 60 μm and an opening of 45 μm. The flow patterns [29] and pressure drop and the outlet vapor quality were studied for FC-72 dielectric liquid as the working fluid.

As mentioned [29, 30] examined the boiling flow of FC-72 in a microgap enhanced with a parallel array of nucleated square pin-fins. The present study aims to address the single-phase and two-phase boiling flow heat transfer of FC-72 in a microgap enhanced with a staggered array of square micro pin-fins nucleated with different pores.

2. Experiment setup

In the present study, the experimental setup, the test module, and the experimental procedure are the same as those reported in details in [29, 30]. Here, the structure of the microgap fins is different from the previous works. In the previous works [29, 30], the pin-fins was in a parallel array, and the pin-fins was also nucleated with an opening of 45 μm. In the present work, the etched pin-fins are in a staggered array and with two different openings of 15 μm and 45 μm. The cross-section of the micro pin-fins is a square with a size of 100 μm, and the height of the pin-fins is also 100 μm. So that the micro pin-fins are cubes of size 100 μm. Inside each of the pin-fins is nucleated by a cylindrical pore of diameter 60 μm. The opening-width of the pores can be 15 μm or 45 μm. A 10 mm $\times$ 10 mm area at the center of the microgap is covered with 613 micro pin-fins and the height of the microgap and pin-fins is 100 μm. A photo of the microgap is depicted in Fig. 1. Fig. 1(a) shows and overall view of the pin-fins enhanced micro gap.

Fig. 1(b) illustrates the back of the microgap with drilled holes for thermocouples. The thermocouple holes are 80 μm wide and 170 μm deep. The thermocopuple holes were filled with thermal grease to minimize the thermal contact resistance. The thermocouples are distributed evenly along the test section. It should be noted that the area of interest is where the pin-fins are etched (see Fig. 1(a)). The hot element is mounted below the surface of the etched pin-fins. Therefore, most of the heat transfer occurs in this area. Due to the symmetry of the microgap along the horizontal line at the model of the thermocouples are placed at one side of the symmetry line to well-cover the test area. The average temperature of the five thermocouples is computed and reported as the temperature of the test area.

Fig. 1(c) depicts some details about the dimensions of the microgap. Fig. 2 depicts the etched pin-fins over the test area. The

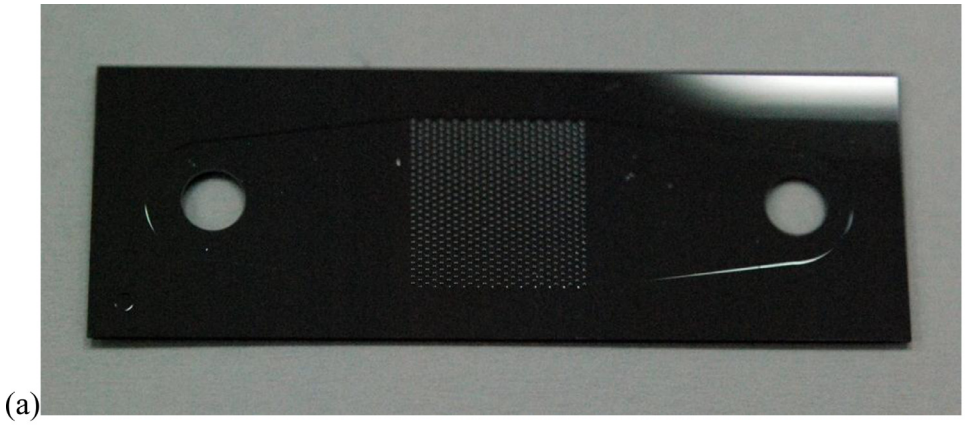

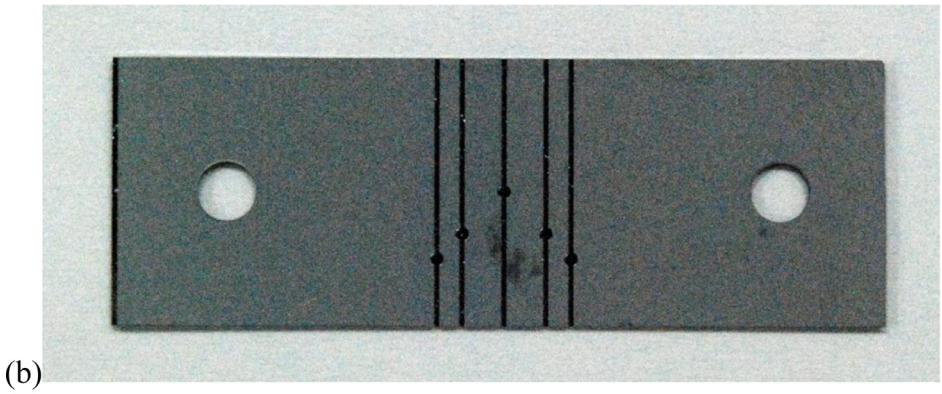

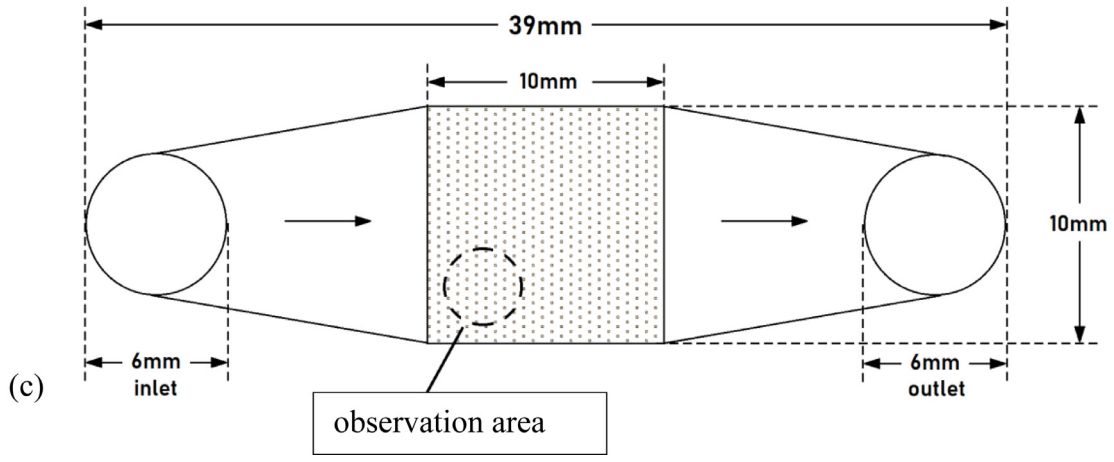

Fig. 1. The microgap and the etched columnar nucleated pin-fins; (a): front view with etched pin-fins; (b): the back view with drilled thermocouples holes; (c): the schematic view of the microgap utilized for single-phase numerical model.

longitudinal and lateral spacing between the pin-fins is 400 μm. Below the enhanced surface of the microgap, there is an element which produces a constant heat flux. The dielectric flow of FC-72 follows in the microgap and absorbs the element heat flux. The outlet is at vacuum pressure as the phase-change temperature the test-section is controlled by the outlet pressure. Indeed, the vacuum pump is employed to control the saturation temperature of FC-72 at the microgap.

The degassing process was required at the beginning of tests to ensure that there is no air in the setup. The de-gassing was performed by the vacuum pump and purging the gas in this state. During the de-gassing process, the heater was increased gradually until the FC-72 boiled at 50 °C for twenty minutes. Then, the control valve of the vacuum port was opened for two to three seconds, with the vacuum pump running to release the non-condensable gases. These heating and degassing procedures were repeated three times. During the experiment, the FC-72 is circulated in a close-loop consisting of a condenser to condense the FC-72 vapor state. Hence, the pure liquid FC-72 enters the test section, and a liquid-vapor of FC-72 leaves the FC-72. The temperature of the mixture was adjusted by controlling the pressure of the test section.

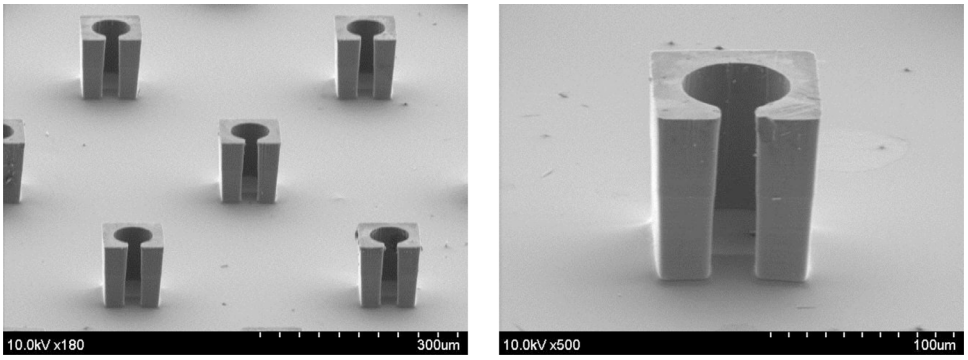

Fig. 2. A photo of etched pin-fins (C-60-15) in a stag grated array over the surface of the microgap.

A Teflon gasket as a layer of insulation is placed beneath the element to separate the stainless steel module from the element thermally. Then, the microgap is placed over the element, and another layer of Teflon was used above the microgap. Hence, the heat of the element will reach the microgap but is separated from the stainless steel module. Moreover, a layer of asbestos is used below the Teflon layer. The whole module is also covered with a thick layer of the insulation-cotton. The heat-losses are estimated by evaluation the difference between the input power by the power supply and the amount of absorbed heat by the working fluid at the output of the test section (the energy difference between the input and output working fluid). The heat-loss is estimated 2–8% of the input power supply.

The measuring instruments of the present study are DC power supply, electronic flowmeter, pressure gauge, differential pressure gauge, and thermocouples. The accuracy and details of the measuring instruments are also well discussed in [29, 30].

3. Single-phase mathematical model

The single-phase flow and heat transfer of FC-72 in the microgap is numerically studied. The convective heat transfer in the liquid is taken into account, and the conjugate heat transfer in pin-fins is neglected. 3D-Meshing inside the pin-fins to consider the conjugate heat transfer in the pin-fins requires a tremendous number of grid points, which is out of our computational capability. The following basic assumptions are employed to model the single-phase flow and heat transfer in the micro gap: 1. The domain of the solution is a three-dimensional Cartesian coordinate system. 2. The working fluid FC-72 is an incompressible Newtonian fluid. 3. The physical properties of the working fluid are all homogeneous and constant. 4. The flow field is a steady-state turbulent flow field, which is analyzed using the realizable k-ε model. 5. The temperature differences are limited, and the thermal radiation effects are negligible.

The temperature range of the single-phase working fluid is 50 °C-75 °C in the simulations. Using the temperature-dependent thermophysical-properties of FC-72 in [30, 32], the relative change in the sensible heat, thermal conductivity, and dynamic viscosity is 4%, 5.%, 3.75%, respectively in the mentioned range of temperatures.

3.1. Governing equations

The governing equations are for continuity and momentum are as follows:

Continuity

$$\frac{\partial \rho}{\partial t} + \frac{\partial}{\partial x_i}(\rho u_i) = 0 \tag{1}$$

Momentum Equation:

$$\frac{\partial}{\partial t}(\rho u_i) + \frac{\partial}{\partial x_j}\left(\rho u_i u_j\right) = -\frac{\partial p}{\partial x_i} + \frac{\partial}{\partial x_j}\left(\mu_e \frac{\partial u_i}{\partial x_j}\right) + F_i \tag{2}$$

where ρ is the fluid density, t is time, u_i is the velocity component in i direction. In Eq. (2), $\mu_e = \mu + \mu_t$ is the sum of the laminar flow and the turbulent viscous coefficient, which is also the effective viscosity coefficient, and F_i is the external body force or the porosity in the i direction. As the buoyancy forces or external fields are negligible, F_i is zero in the present study. The heat equation, the turbulent kinetic energy equation, and the turbulent kinetic energy dissipation ratio are as follows:

Energy equation

$$\frac{\partial}{\partial t}(\rho c_p T) + \frac{\partial}{\partial x_i}(\rho c_p T u_i) = -p\frac{\partial u_i}{\partial x_i} + \frac{\partial}{\partial x_i}\left(k_\varepsilon \frac{\partial T}{\partial x_i}\right) + \mu \emptyset + S_\varepsilon \tag{3}$$

Turbulent kinetic energy equation

$$\frac{\partial}{\partial}(\rho k) + \frac{\partial}{\partial x_j}\left(\rho k u_j\right) = \frac{\partial}{\partial x_i}\left[\left(\mu + \frac{\mu_i}{\sigma_k}\right)\frac{\partial k}{\partial x_i}\right] + G_k - \rho\varepsilon \tag{4}$$

Turbulent kinetic energy dissipation ratio

$$\frac{\partial}{\partial t}(\rho\varepsilon) + \frac{\partial}{\partial x_j}\left(\rho\varepsilon u_j\right) = \frac{\partial}{\partial x_i}\left[\left(\mu + \frac{\mu_t}{\sigma_\varepsilon}\right)\frac{\partial \varepsilon}{\partial x_i}\right] + C_{1\varepsilon}G_k\frac{\varepsilon}{k} - C_{2\varepsilon}\rho\frac{\varepsilon^2}{k} \tag{5}$$

where T, k, and ε are the temperature, turbulent kinetic energy, and turbulent kinetic energy dissipation ratio, respectively. The specific heat capacity is denoted by Cp, and the effective thermal conductivity indicated by k_ε. Here, G_k is the turbulent flow energy produced by the average velocity gradient, which is defined as follows:

$$G_k = -\rho\overline{u_i' u_j'}\frac{\partial u_j}{\partial x_i} \tag{6}$$

Model constants are $C_{1\varepsilon} = 1.44$, $C_2 = 1.9$, $\sigma_\kappa = 1.0$, $\sigma_\varepsilon = 1.2$.

3.2. Boundary conditions

The flow enters the microgap through the 1 mm diameter inlet port with the inlet velocity of V_{in}. The inlet velocity is calculated based on the flow rate and the surface area of the inlet port. The flow rate varies in the range of 6~31 ml/min in the present study. The inlet temperature is et to 50 °C, and the inlet turbulence intensity (I) is evaluated using the Reynolds number as follows:

Table 1
The error analysis of various grid sizes.

	Case 1	Case 2	Case 3	Case 4	Case 5	Case 6	Case 7
Number of grids	4,602,570	7,563,658	17,201,969	21,246,341	31,266,872	43,458,982	57,346,570
Error(%)	0.09369	0.13722	0.11306	0.03028	0.04493	0.05713	–

$$Re_{D_H} = \frac{D_H \times V_{in} \times \rho}{\mu} \tag{7}$$

$$I = 0.16(Re_{D_H})^{-0.125} \tag{8}$$

where ρ and μ are the density and dynamic viscosity of FC-72, respectively. The hydraulic diameter of the microgap (D_H) is evaluated as

$$D_H = \frac{4A_c}{P_{ch}} \approx 198\mu\text{m} \tag{9}$$

where A_c is the channel cross-section, and P_{ch} is the wet perimeter of the channel. Hence, $D_H = 2(W \times H)/(W + H)$ where W is the channel width, and H is the channel height. The impermeability and no-slip velocity are considered for all of the microgap walls and pin-fins surfaces.

The outlet pressure is set at 79.54 kPa which is the saturation temperature of FC-72 at 50 °C. The back of the microgap (the back of pin-fin enhanced surface) there is an electrical heater with a power of W. The black square in Fig. 3(b) is the location of the element which produces the uniform heat flux of q. The heat flux of q is evaluated by dividing the element power W to the surface area of the element (10 mm × 10 mm). The sidewalls of the microgap as well as the top wall and bottom wall (with no heater element) are well insulated and considered adiabatic. The density of FC-72 at 50 °C is 1631.48 kg/m^3. The opening of pin-fins is always toward the flow direction. Indeed, the flow first reaches the back of a pin-fin with no opening.

3.3. Numerical method and grid check

ANSYS FLUENT is utilized to solve the governing equation of the model in the microgap. A grid check was performed to ensure that the results are independent of the grid resolution. The effect of grid size on the pressure drop was monitored. It is found that a grid above 6 million cells can provide sufficient accuracy. The conduction of the pin fin has been ignored in the numerical simulation. A much larger number of grids would be needed in the simulation of conduction inside the pin fins. However, the main purpose of the simulation is to obtain the fluid flow and pressure distribution around the pin fins. The flow field simulated in this study is dominated by the convection term. The temperature differences are limited, and hence, the radiation effects are negligible compared to the convective heat transfer. Therefore, in order to make the numerical simulation highly accurate and convergent, the discrete method of convection and diffusion term selects the Second Order Upwind algorithm. Since the flow velocity of this study is much lower than the subsonic velocity and is an incompressible flow, the pressure-based solver (Pressure-Based Solver) is selected, and the iterative methods of velocity and pressure coupling are adopted as the Semi-Implicit Method for Pressure Linked Equations-Consistent (SIMPLEC) algorithm.

The purpose of the grid check analysis is to balance the numerical accuracy and computational time. A low number of grid points reduced the numerical accuracy of the results, while too many grid-points increase the computational costs dramatically. In order to study the effect of grid size on the accuracy of the results, 13 monitor points are selected along the test surface. The monitor points are depicted in Fig. 4. The grid check is performed for the case of C-60-5 at 35 °C. The number of grids and the relative temperature error, compared to the case 7 with the finest grid size, are reported in Table 1. The change of accuracy shows an oscillation behavior. This oscillation behavior, which can be due to the effect of grid resolution in the domain and boundaries. There are many pin-fins with detailed geometry considerations. Many of the grids are the boundary grids, and reducing the size of the grid affects both the boundary grids and the domain grids, and these two grid sizes shall be matched in the domain of solution. Hence, an oscillating behavior can be expected. However, for the grid size of Case 4 and lower, the results are within acceptable accuracy for most engineering applications. As seen case 4 provides the results with only 0.03% relative error, which is acceptable in most engineering analyses and designs. Hence, the grid of case 4 is accepted for computations of the present study. A view of the grid around several pin-fins and around a pin-fin is depicted in Fig. 5.

4. Results and discussion

In the present study, the two-phase flow is solely studied experimentally; however, the single-phase flow is investigated numerically and experimentally. The reason for performing the single-phase flow was the fact that the onset of nucleation boiling is very important in the present design. At the onset of nucleation boiling the flow and heat transfer can be assumed single-phase flow. Hence, the onset of nucleation boiling is under direct influence of single-phase flow and heat transfer. The numerical data for pressure distribution and streamlines are utilized to understand the effect of the presence of pin-fins on the flow and heat transfer at the onset of nucleation boiling and understand the possible underlying physics of experimental observations for two-phase flow boiling. Thus, the results of the present study are presented in two-part. The first part is the simulation results for the flow and heat transfer of FC-72 in the microgap. The second part is the experimental results of two-phase flow boiling heat transfer in the microgap.

4.1. Simulation results for single-phase flow

This section discusses the results of single-phase thermal convection numerical simulation analysis of the above two types of heat sink microgaps. Before starting the numerical investigation, the correctness of the numerical model is tested against the experimental data of the present study for the case of C-60-45 at 50 °C. The comparison is performed for various values of the inlet flow rate of FC-72 in the range of 6 to 31 ml/min when the surface heat flux was 4 W/cm^2. In this case, the temperature difference between the inlet temperature and the average surface temperature (ΔT) was reported as a function inlet flow rate in Fig. 6 for both the experimental measurements and numerical simulation.

After analysis of the results, the maximum error occurs at an inlet flow rate of 6 ml/min, which is about 69.58% while the minimum error occurs at an inlet flow rate of 20 ml/min with a value about 0.44%. The conduction of the pin fin has been ignored in the present numerical simulation. Hence, the effective surface area is underestimated, and the wall temperature is expected to be overestimated. The larger difference between the numerical and experimental data at a low flow rate can be due to the insulation problem. When the flow rate is low, the temperature of the test sur-

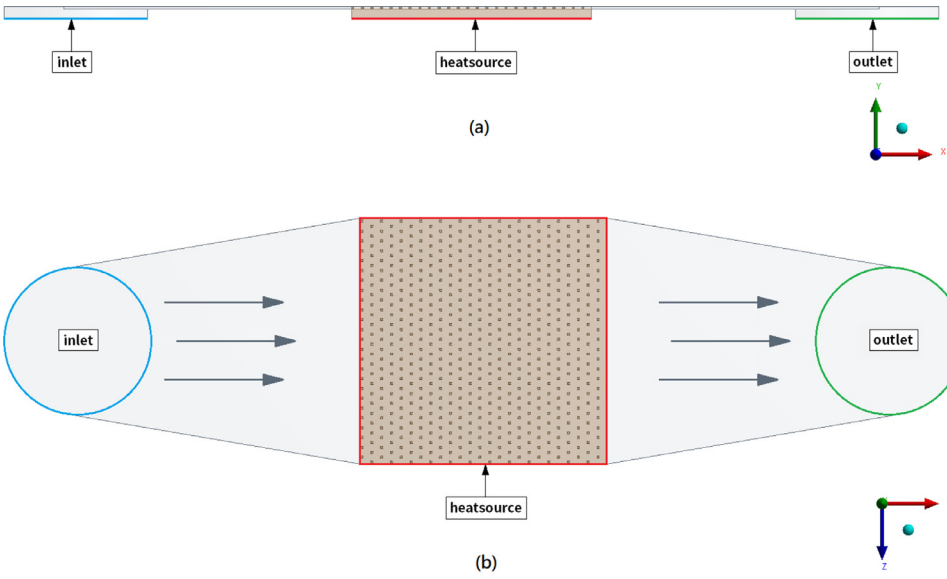

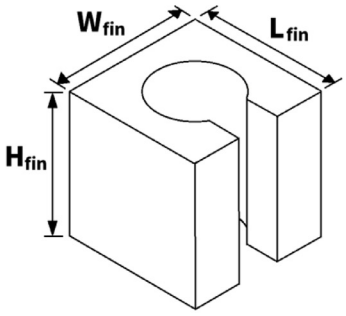

(c)

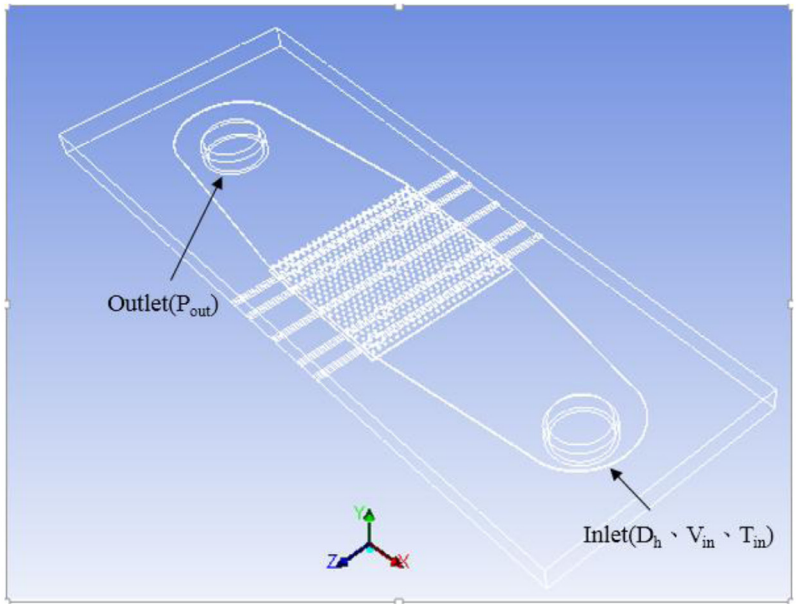

(d)

Fig. 3. The produced model in Ansys-Fluent workbench; (a): side view the location of hot element, inlet, and outlet boundary conditions; (b): top view the location of hot element, inlet, and outlet; (c): dimensions of microgap; (d): wireframe 3D model of microgap including the thermocouple locations.

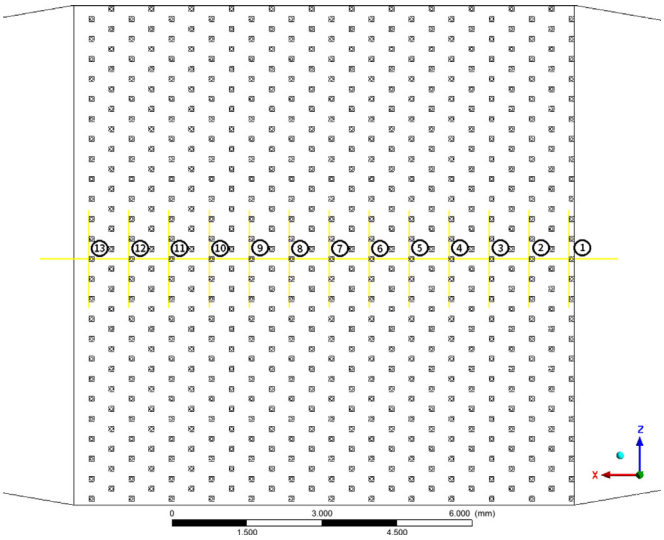

Fig. 4. The location of the 13 monitor points for grid check.

Table 2
Maximum pressure (Pa) at pin fin for different configurations at different flow rates.

		6 (ml/min)	12 (ml/min)	20 (ml/min)	31 (ml/min)
$T_{in} = 35$	C-60-5	47,436.89	49,616.64	53,082.08	58,768.54
	C-60-15	47,438.38	49,618.85	53,088.14	58,770.48
	C-60-30	47,438.71	49,618.39	53,086	58,776.48
	C-60-45	47,437.51	49,610.45	53,058.63	58,726.63
$T_{in} = 50$	C-60-5	81,068.34	82,975.48	86,039.83	92,045.12
	C-60-15	81,069.96	82,977.59	86,045.69	91,854.33
	C-60-30	81,070.16	82,977.09	86,043.77	91,856.65
	C-60-45	81,068.86	82,966.58	86,017.02	91,820.91

face is higher, which boosts the heat losses from the setup insulations. Moreover, when the flow rate is low, any heat losses can change the setup temperature significantly. By the increase of flow rate, the error between the experimental results decreases until it reaches a minimum value of 20 ml/min. After this point, the error starts to rise smoothly, which can be due to the intensification of the turbulence effects. Although the error between the simulation and experimental values are high in some cases, the consistency of the trend of the results shows that the simulation results have certain credibility and reference value.

Fig. 7(a) and (b) show the pressure distribution for the case of C-60-45 and C-60-15, respectively. Table 2 summarizes the max-

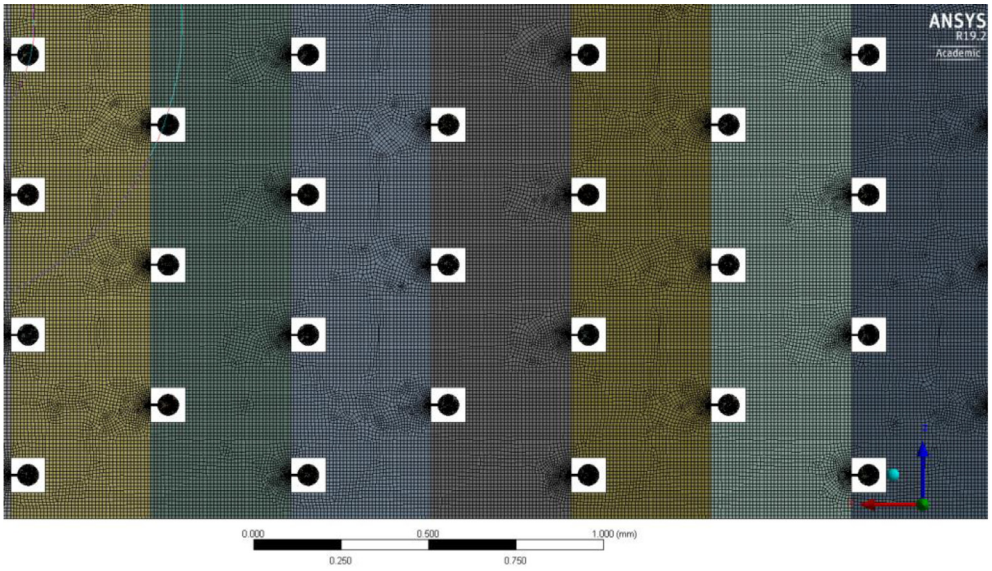

(a):

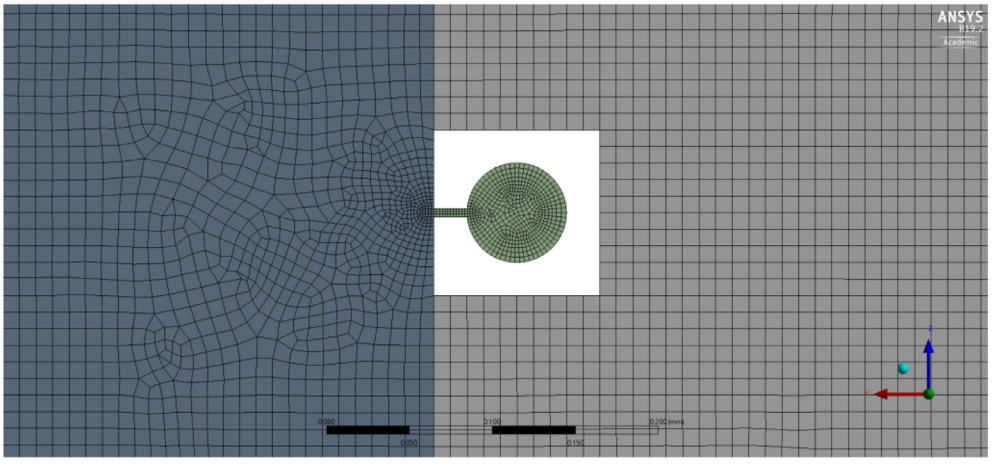

(b):

Fig. 5. A view of the utilized grid for case 4; (a): a general view; (b): a zoomed view.

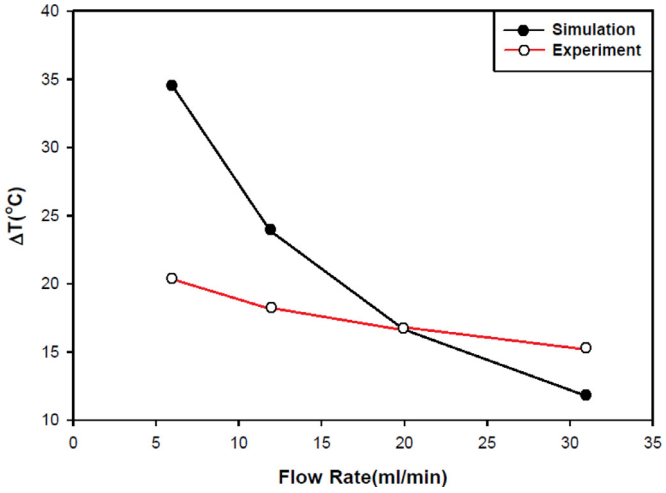

Fig. 6. Comparison of numerical simulation and experimental measurement.

Table 3
The average temperature of the pin-fin for various values of the flow rate and working temperature.

		6 (ml/min)	12 (ml/min)	20 (ml/min)	31 (ml/min)
T_{in} = 35 °C	C-60-5	71.2046	59.72	52.2608	46.4078
	C-60-15	70.8364	59.4338	52.117	46.2474
	C-60-30	71.0688	59.6424	52.2772	46.4538
	C-60-45	70.9466	59.561	51.5364	44.8366
T_{in} = 50 °C	C-60-5	86.7292	74.6006	66.8638	59.5638
	C-60-15	86.3038	74.2614	66.634	59.2408
	C-60-30	86.7344	74.3096	66.8814	59.4544
	C-60-45	86.4458	74.3782	65.6212	58.3418

Table 4
The tested mass fluxes (kg/m^{2}s) in the microgap.

Flow rate [ml/min]	Mass flux at T_{sat} = 50 °C	Mass flux at T_{sat} = 35 °C
6	93	97
12	138	142
20	196	200
31	275	284

imum pressure inside the pin-fin cavity at various flowrate and temperatures. Fig. 8 shows a zoomed view of the velocity vectors at micro pin-fins for the two cases of C-60-45 and C-60-15. As seen, the pressure across the micro-cap drops gradually. In the case of C-60-45, the pressure drop mostly occurs in the pin-fin section of the microgap. The maximum pressure in the case of C-60-5 is slightly higher than that of C-60-15.

Figs. 8 and 9 compare the velocity vectors and magnitudes of the flow at the pin-fin scale. Interestingly, there is a notable vortex at the opening of C-60-45, and the velocity vectors and magnitudes are very weak inside the cavity pin fins. In the case of C-60-15 with a smaller opening, the vortex at the opening is weaker, and the streamlines are smoothly stronger inside the cavity. Moreover, in the case of C-60-45 low-pressure area in the pin-fin cavity and outside the pin-fin is wider, and the pressure is also lower compared to the case of C-60-15. Fig. 9 depicts that a longer area after pin-fins with a smaller opening is under the influence of the pin fin.

Fig. 10 depicts the temperature distribution in the microgap for two cases of C-60-45 and C-60-15 for a high flow rate of 20 ml/min and saturation temperature of T_{sat} = 50 °C. This figure interestingly shows that the temperature inside the pin fin cavity with a smaller opening is higher than that with a larger opening. The flow around the pin fin of C-60-15 is slightly hotter than that of C-60-45. The average temperature of the pin-fin is summarized in Table 3 for various flow rates and working temperatures. Table 3 also shows a higher pin-fin temperature in the case of C-60-15. Note that the conduction of the pin fin has been ignored. Hence, the wall temperature is expected to be overestimated in the present simulation.

4.2. Experimental study of boiling flow and heat transfer

In this section, the boiling heat transfer in the micro-pin-fin enhanced microgap is examined experimentally for two opening pore sizes of 15 μm and 45 μm as well as various mass fluxes. Moreover, the effect of two saturation boiling temperatures of T_{sat} = 35 °C and T_{sat} = 50 °C on the boiling heat transfer of the microgap is addressed. The details of the examined FC-72 flow rate and corresponding mass flux are summarized in Table 4. During the experiments, the element heat flux varies in the range of 0.2–10 W (0.2–10 × 10^4 W/m^2). The heat flux starts from low values and gradually increases until the surface temperature exceeds 100 °C or the pressure drop reaches 15 kPa or higher.

4.2.1. The surface-superheat temperature

Fig. 11 illustrates the relation of the surface-superheat temperature and surface heat flux for different magnitudes of mass flux in the case of C-60-15 and saturation temperature of T_{sat} = 50 °C. As shown in the figure, when the mass flux is low (94 kg/m^{2}s), the nucleate boiling arises at small values of surface heat flux (≦4.22 W/cm^2) and with on boiling superheat temperature of

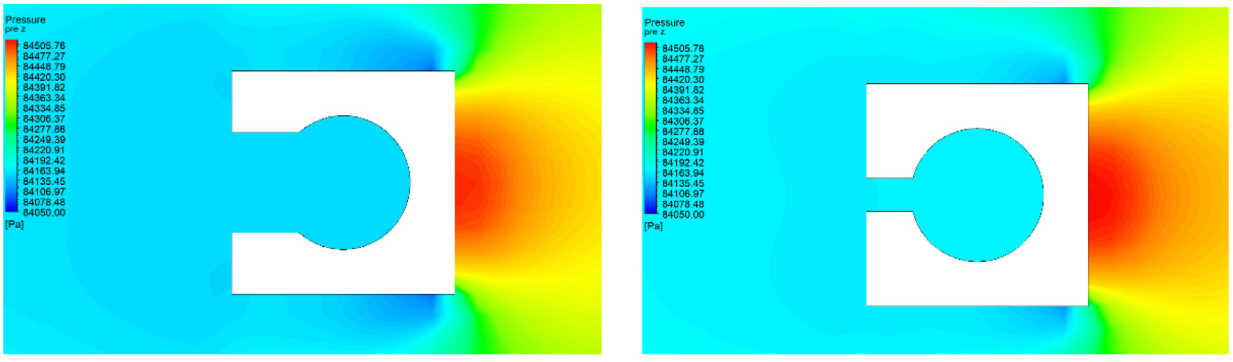

Fig. 7. Contours of pressure distribution in the microgap for a mass flux of 20 ml/min (196 kg/m^{2}s), and T_{sat} = 50 °C, (a): surface structure of C-60-45, (b): surface structure of C-60-15.

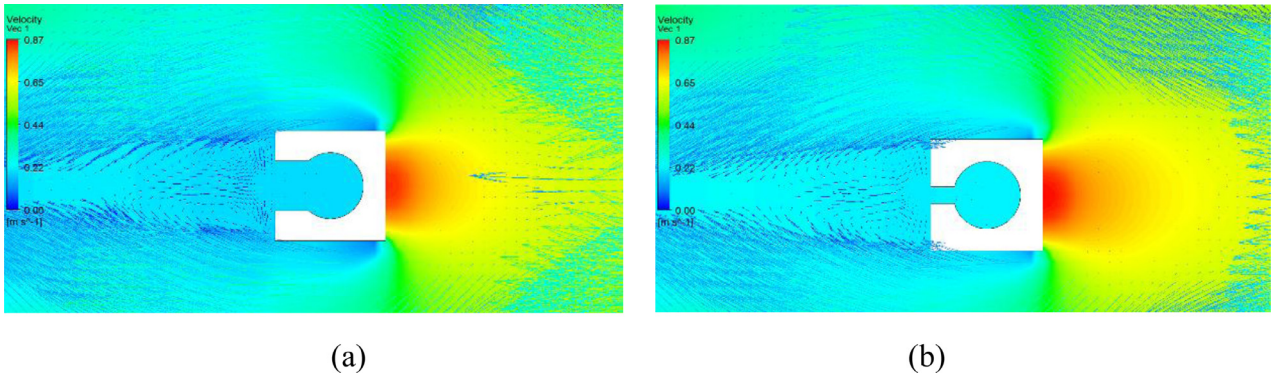

Fig. 8. A zoomed view of velocity vectors at a micro pin-fins for a flow rate of 20 ml/min (196 kg/m^{2}s), and T_{sat} = 50 °C, (a): surface structure of C-60-45, (b): surface structure of C-60-15.

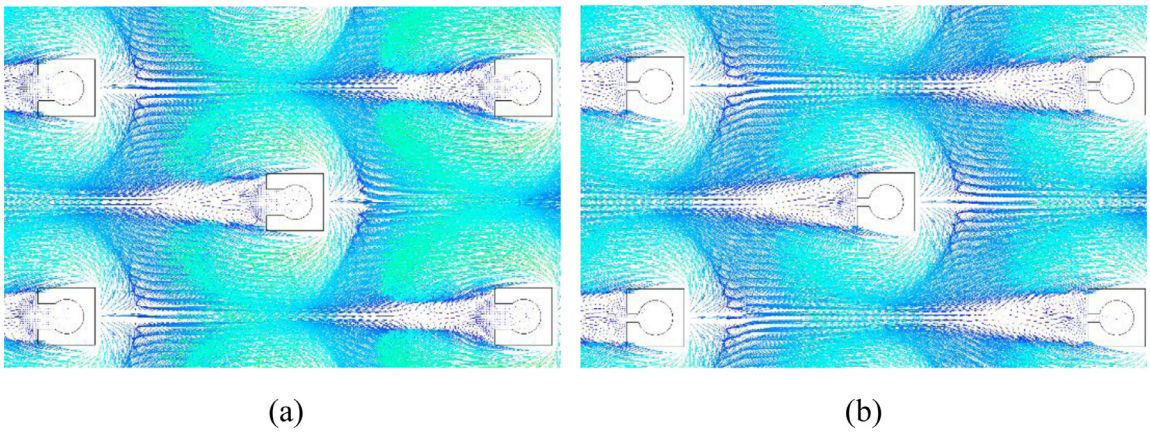

Fig. 9. A general view of the velocity vectors at micro pin-fins for a flow rate of 20 ml/min (196 kg/m^{2}s), and T_{sat} = 50 °C, (a): surface structure of C-60-45, (b): surface structure of C-60-15.

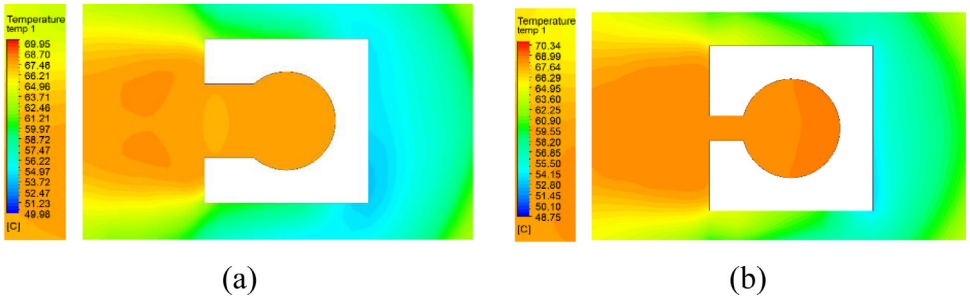

Fig. 10. Temperature distribution at micro pin-fins for a flow rate of 20 ml/min (196 kg/m^{2}s), and T_{sat} = 50 °C (a): surface structure of C-60-45, (b): surface structure of C-60-15.

ΔT_{ONB} = 20.15 °C. The low corresponding heat flux for on boiling temperature is due to the low mass flux of FC-72, and hence, the low sensible heat capacity of the flow. In this case, the temperature of the single-phase flow rises sharply, and boiling occurs at a low heat flux.

When the mass flux rises to 138 kg/m^{2}s, the boiling commences at an upper surface heat flux, ($q'' \leqq$ 6.41 W/cm^2). By the increase of mass flux from 94 kg/m^{2}s to 138 kg/m^{2}s, the superheat temperature for onset of boiling increases from 20.15 °C to 31.84 °C. The increase of superheat temperature and mass flux increases the sensible single-phase flow heat capacity, and hence, as it was observed the surface heat flux at the onset of boiling increases from 4.22 W/cm^2 to 6.41 W/cm^2 by the increase of the mass flux from 94 kg/m^{2}s to 138 kg/m^{2}s. The reason is attributed to the fact that there is a competition between the flow hydrodynamics effects, low-pressure sites, and the nucleation formation. Indeed, when the pressure is uniformly high around the pin-fins, and there is a moderated hydrodynamic interaction between the surface of pin-fins and the liquid, the formation of nucleation and development of bubbles delays to a higher superheat temperature. This happened at a moderate mass flux of 138 kg/m^{2}s. At a lower mass flux, the hydrodynamic interaction between the pin-fins is lower, and the nucleation can be formed and developed. As a higher mass flux, the hydrodynamic interaction between the pin-fins and the liquid raises, but there are also low-pressure areas in the cavity of pin fins, which are perfect sites for nucleation formation and bubble development. Hence, the superheat temperature of 31.84 °C for the case of 138 kg/m^{2}s can be considered as a critical situation that can benefit neither from the low hydrodynamic interaction of the liquid with pin fins nor the low-pressure sites in the cavity of the pin-fins.

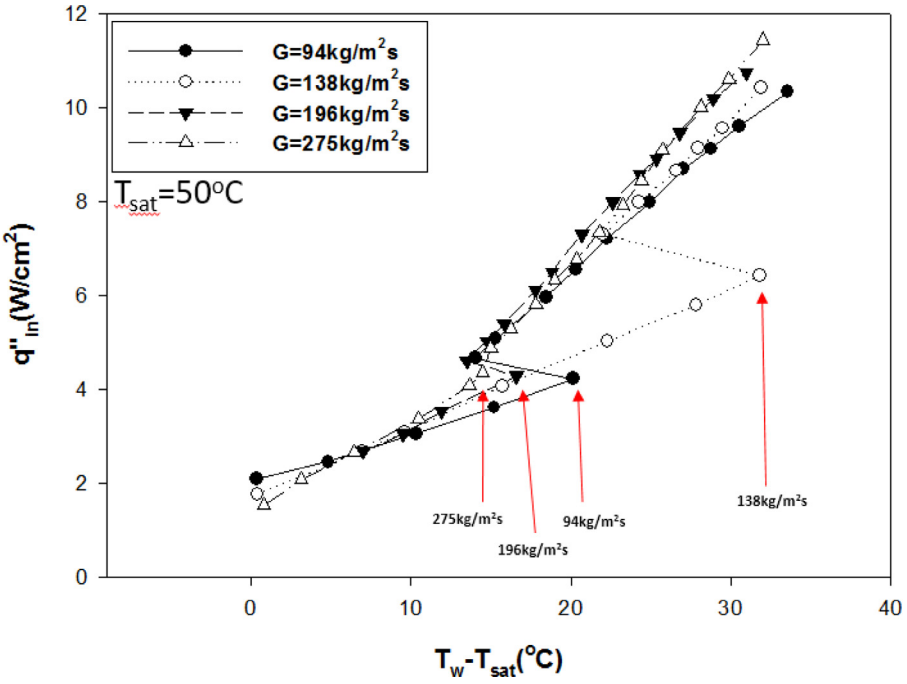

Fig. 11. Surface-superheat temperature (T_w-T_{sat}) and surface heat flux curves for different magnitudes of FC-72 mass flux for the case of C-60-15 and saturation temperature of T_{sat} = 50 °C.

At the onset of boiling heat transfer, the nucleate boiling commences at the downstream of the micro pin-fin surface. By the increase of heat flux, the temperature superheats increases. After flow boiling, the increase in the surface-superheat is steeper than that of the single-phase, indicating that the heat transfer coefficient is significantly improved.

When the mass flux rises to higher values of 196 kg/m^{2}s and 275 kg/m^{2}s, the trend of the results is in agreement with the case of 138 kg/m^{2}s for single-phase flow heat transfer, so the superheat temperature elevates by the raise of the surface heat flux. However, the onset of boiling heat transfer occurs at lower heat flux and superheat temperature. The corresponding surface-superheat temperatures for the cases of 196 kg/m^{2}s and 275 kg/m^{2}s are ΔT_{ONB}=15.82 °C and ΔT_{ONB} = 14.99 °C, respectively. This is an interesting result that shows the effect of the micro-pin-fins and the structure of cavities in the pin-fins. Indeed, when the mass flux and accordingly, the flow velocity increases, the effect of surface structure on the flow hydrodynamic intensifies. The nucleation boiling starts from the low-pressure areas, and the onset of flow-boiling occurs at a lower superheat temperature. Therefore, the surface-superheat of the test surface reduces with the raise of the mass flux when the mass flux is high.

Fig. 12 is a graph of surface-superheat and heat flux of C-60-15 and C–N–N at a saturation temperature of 50 and 35 °C. This figure interestingly shows that the surface superheat temperature of T_{sat} = 35 °C is notably lower than that of T_{sat} = 50 °C. This is presumably because of the difference between the physical properties of FC-72 at 35 °C and 50 °C. Indeed, the viscosity coefficient and the surface tension coefficient of FC-72 at 35 °C are about 17.5% and 14.8% higher than that at 50 °C, respectively. The curves of C–N–N surface having solid pin fins without opening at 50 °C are compared with C-60-15. As shown in Fig. 12, the ONBs of C–N–N are significantly higher than those of C-60-15 for either 94 kg/m^{2}s or 196 kg/m^{2}s.

Fig. 13 shows the heat flux and convective heat transfer coefficient of C-60-15 at the saturation temperatures of T_{sat} = 35 °C and T_{sat}=50 °C. It can be observed that the heat transfer coefficient of 35 °C is better than 50 °C, regardless of the value of mass flux. This is presumably due to the physical properties of FC-72 at 35 °C, which facilities the flow boiling. The heat capacity and phase change latent heat of FC-72 at 35 °C are much higher than that of 50 °C. The temperature-dependent thermophysical properties of FC-72 are listed in [30].

4.2.2. The size of pore opening

Fig. 14 is a graph of surface-superheat and surface heat flux for two surface structures of C-60-15 and C-60-45. The horizontal axis is the surface-superheat, and the vertical axis is the surface heat flux. It can be seen from the figure that the superheat degree required for initial boiling on the surface structure of C-60-15 (ΔT_{ONB} = 20.14 °C@94 kg/m^{2}s and 31.81 °C@138 kg/m^{2}s) is higher than that of C-60-45 (ΔT_{ONB} = 18.65 °C@94 kg/m^{2}s, 25.61 °C@138 kg/m^{2}s) at a low mass flux (G = 94–138 kg/m^{2}s). This is because the structure of the pin-fins does not affect the flow hydrodynamic at low mass fluxes. Moreover, the nucleation of fin fins (making a cavity inside the pin-fins) increases the thermal resistance of the fins, and consequently, it leads to the growth of the temperature difference between the surface and the working fluid. By the increase of mass flux, the effect of the structure of pin-fins on the flow hydrodynamic gets important, and the flow boiling temperature drops significantly. In the case of high mass flux of 196 kg/m^{2}s, the reduction in the nucleation pore opening from 45 μm (C-60-45) to 15 μm (C-60-15) reduces the boiling surface heat temperature from ΔT_{ONB} = 20.06 °C to ΔT_{ONB} = 16.62 °C. This is because the pore opening of C-60-15 the temperature inside the cavity fin is higher, and hence, the bubbles can be generated easily.

4.2.3. Heat transfer and pressure drop

Figs. 15 and 16 respectively depict the convective heat transfer coefficient and pressure drop as a function of surface heat flux for various mass heat fluxes and two fin structures of C-60-15 and C-60-45 at saturation temperature of T_{sat} = 50 °C. For a high magnitude of the mass flux (196 kg/m^{2}s), the larger the opening structure, the better the single-phase convective heat transfer coefficient. Considering a constant surface heat flux of 4.28 W/cm^2,

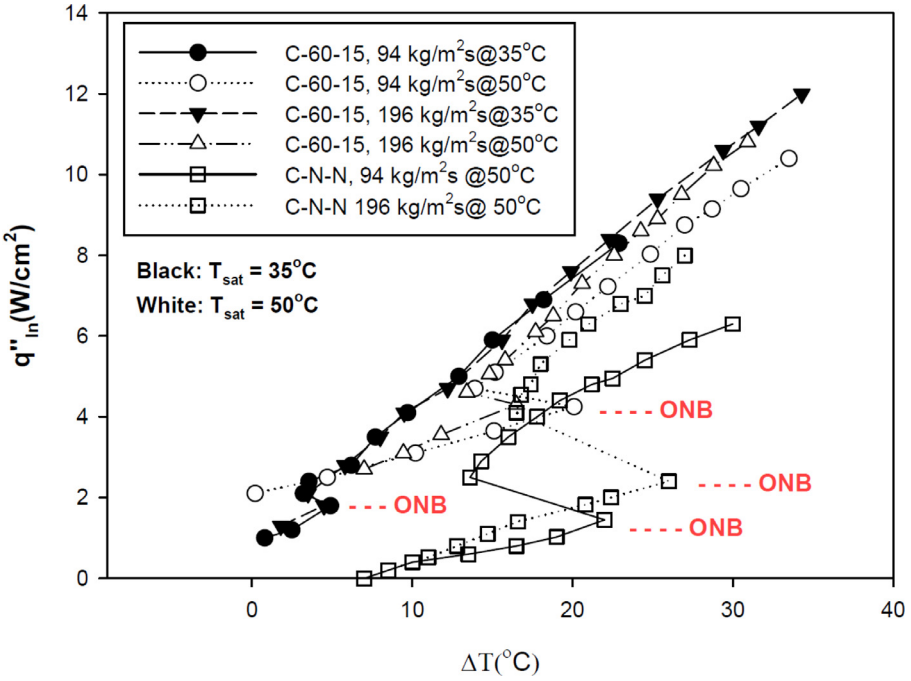

Fig. 12. Surface-superheat temperature ($\Delta T = T_w$-T_{sat}) and surface heat flux curves for different magnitudes of FC-72 mass flux for the case of C-60-15 and C–N–N at saturation temperatures of T_{sat} =35 °C and T_{sat} =50 °C.

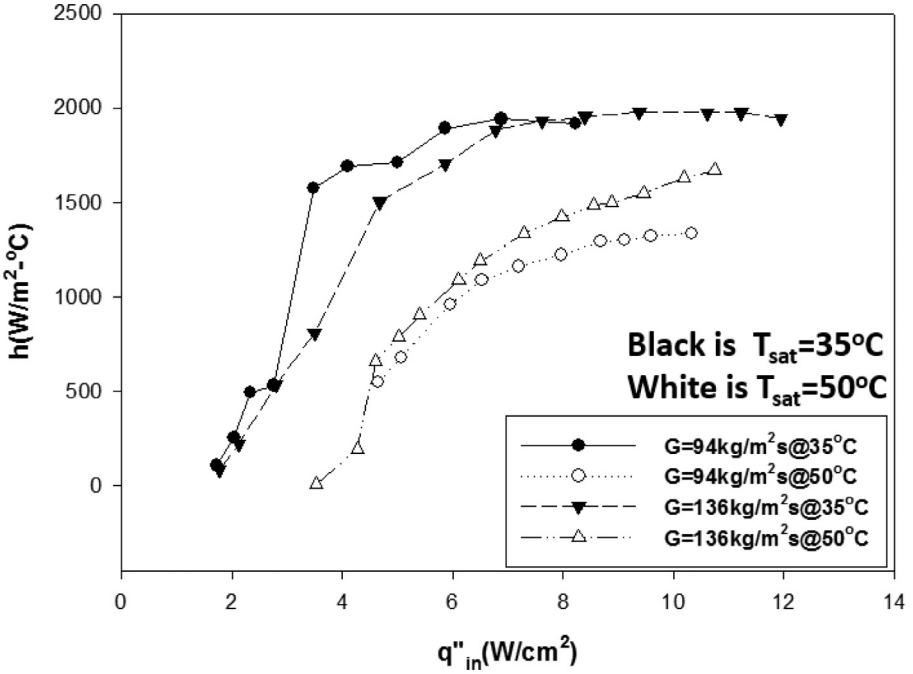

Fig. 13. The convective heat transfer coefficient as a function of surface heat flux at two saturation temperature of T_{sat} = 35 °C and T_{sat} = 50 °C in the case of C-60-15.

the case of C-60-15 shows a boiling flow heat transfer with a large heat-transfer coefficient while the larger opening structure of C-60-45 still is at the single-phase heat transfer with much lower convective heat transfer coefficient. Considering a fixed surface heat flux of 6.1 W/cm^2, both pin-fin structures of C-60-15 and C-60-45 are in two-phase boiling heat transfer regime with solely 3.07% difference in convective heat transfer coefficient. For a higher surface heat flux, both pin-fin structures exhibit an almost identical trend of behavior with the same slope. Hence, it can be concluded that the change in the pore opening is not much effective for high flow mass fluxed and high surface heat fluxes. However, it is effective for the onset of boiling heat transfer and surface-superheat temperatures. Indeed, when the boiling heat transfer commences, the flow disturbs effectively and regardless of the detail of surface structure, the boiling heat transfer continues.

As mentioned, Fig. 16 illustrates the pressure drop across the microgap. This figure demonstrates that a pin-fin structure with a smaller opening (C-60-15) provides a lower pressure drop across the microgap in the single-phase flow regime. In most cases of the two-phase flow boiling, the structure of C-60-15 leads to a lower pressure drop compared to that of C-60-45. This is because of the extensive effect of C-60-45 on the downstream flow, as discussed

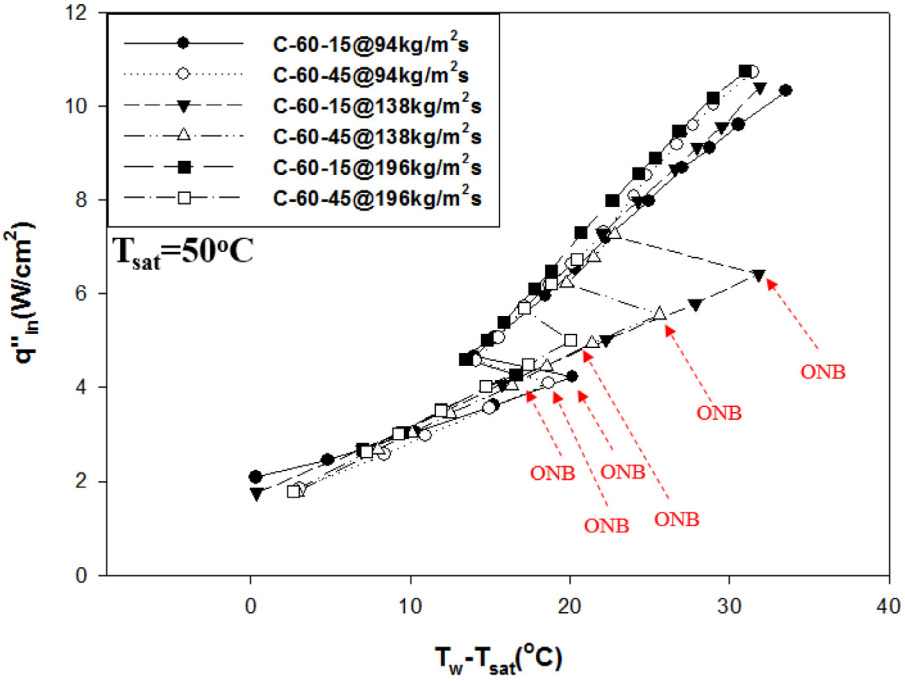

Fig. 14. The relation between the surface-superheat temperature and surface heat flux for both pin-fin structures of C-60-15 and C-60-45 when T_{sat} = 50 °C.

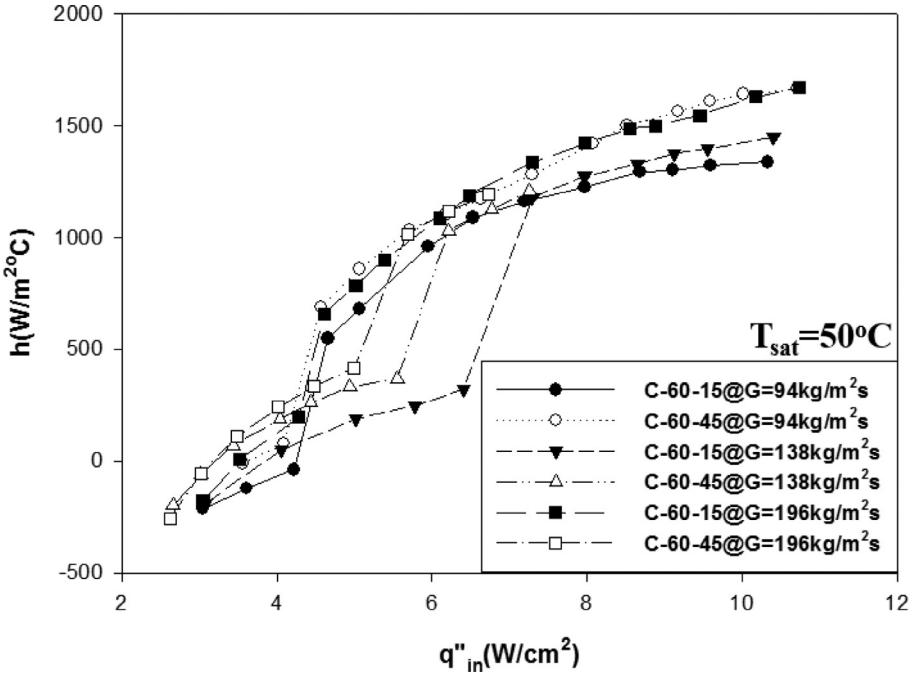

Fig. 15. The convection heat coefficient and the pressure drop as a function of surface-superheat flux for both pin-fin structures of C-60-15 and C-60-45 when T_{sat} = 50 °C.

in single-phase numerical results of Fig. 9. A comparison of the results with a parallel arrangement of micro pin fins of C-60-45 [30] shows that the single-phase pressure drop of parallel array is higher than that of staggered array. For example, in the case of G = 196 kg/m^{2}s, the pressure drop was about 5.8 kPa [30], while in the present study it is about 3.5 kPa.

4.2.4. Flow spectrum analysis

In this experiment, the bubble nucleation and flow field changes were observed by video recording during the initial boiling. Fig. 17 shows the boiling bubble diagram of the test surface for the pin-fin structure of C-60-15 and mass flux of G = 94 kg/m^{2}s at a saturation temperature of T_{sat} = 50 °C. This figure illustrates that the test surface-superheat increases as the surface heat flux rises. By the rise of the surface heat flux and surface-superheat temperature, the flow field changes from single phase to two phases of boiling flow. The transition occurs at the onset of boiling superheat temperature of ΔT_{ONB} = 20.1 °C with a bubbly flow. Just after the onset of the boiling and by a small grow of the surface heat flux, flow regime is bubbly/slug flow. Then, by gradual increase of

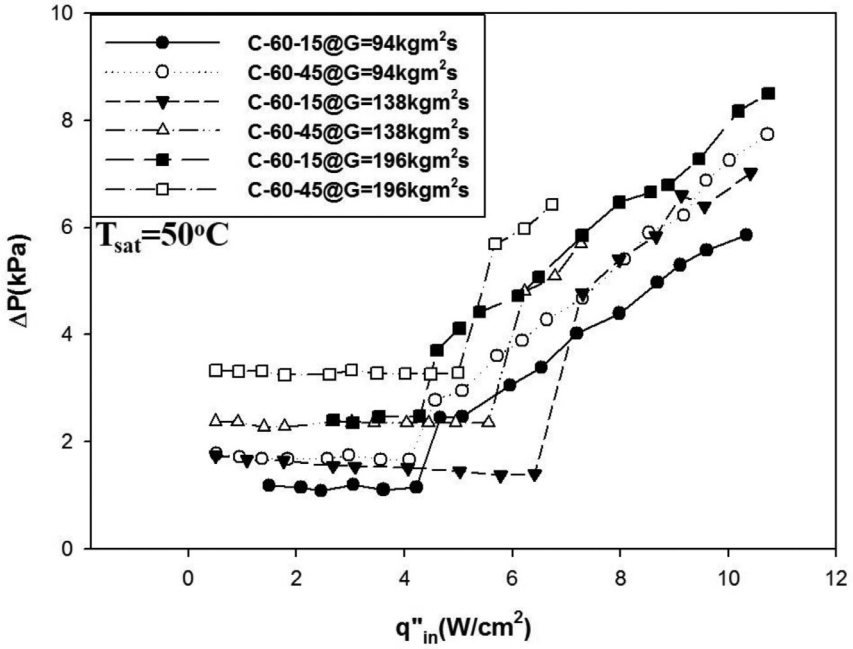

Fig. 16. The pressure drop aginst the surface heat flux for both pin-fin structures of C-60-15 and C-60-45 when T_{sat} = 50 °C.

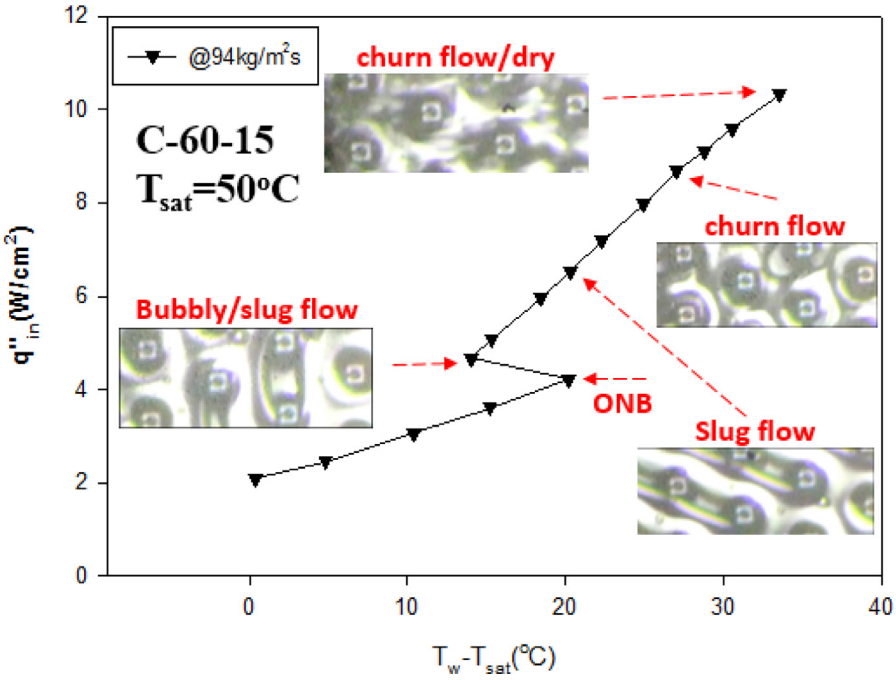

Fig. 17. Boiling bubble diagram of test surface for the case of C-60-15 and mass flux of G = 94 kg/m^{2}s when T_{sat} = 50 °C.

the surface heat flux the flow regime changes to slug flow, churn flow and churn flow/dry flow field. This trend of flow field by the increase of surface heat flux is in agreement with the change of flow spectrum in a tube [33].

Fig. 18 shows the spectrum of flow boiling for a mass flux of G = 138 kg/m^{2}s when the surface heat flux is 4.66 W/cm^2. The results are obtained with a high-speed camera with a shooting speed of 1200 fps. In Fig. 16, the boiling flow spectrum is investigated for 28 ms (t~t + 28 ms). When the liquid flows into the test surface, it will accumulate at the downstream of the fin to form a liquid ball (t + 1 ms), and then the liquid continually absorbs the heat from the fin. The gas gradually generates around the fin and gas area enlarges (t + 2~3 ms), and the liquid flows through the fine branch between the gas bubbles. At this time, the flow field type is called a cell flow. The gas expansion cuts off the cell flow (t + 5 ms). At this time, there are three vacuoles after the truncation. As time passes, some vacuoles are carried downstream, and some vacuoles enter the liquid column next to the fins (t + 14 ms), then a large amount of liquid flows into this zone (+26 ms), forming a cycle.

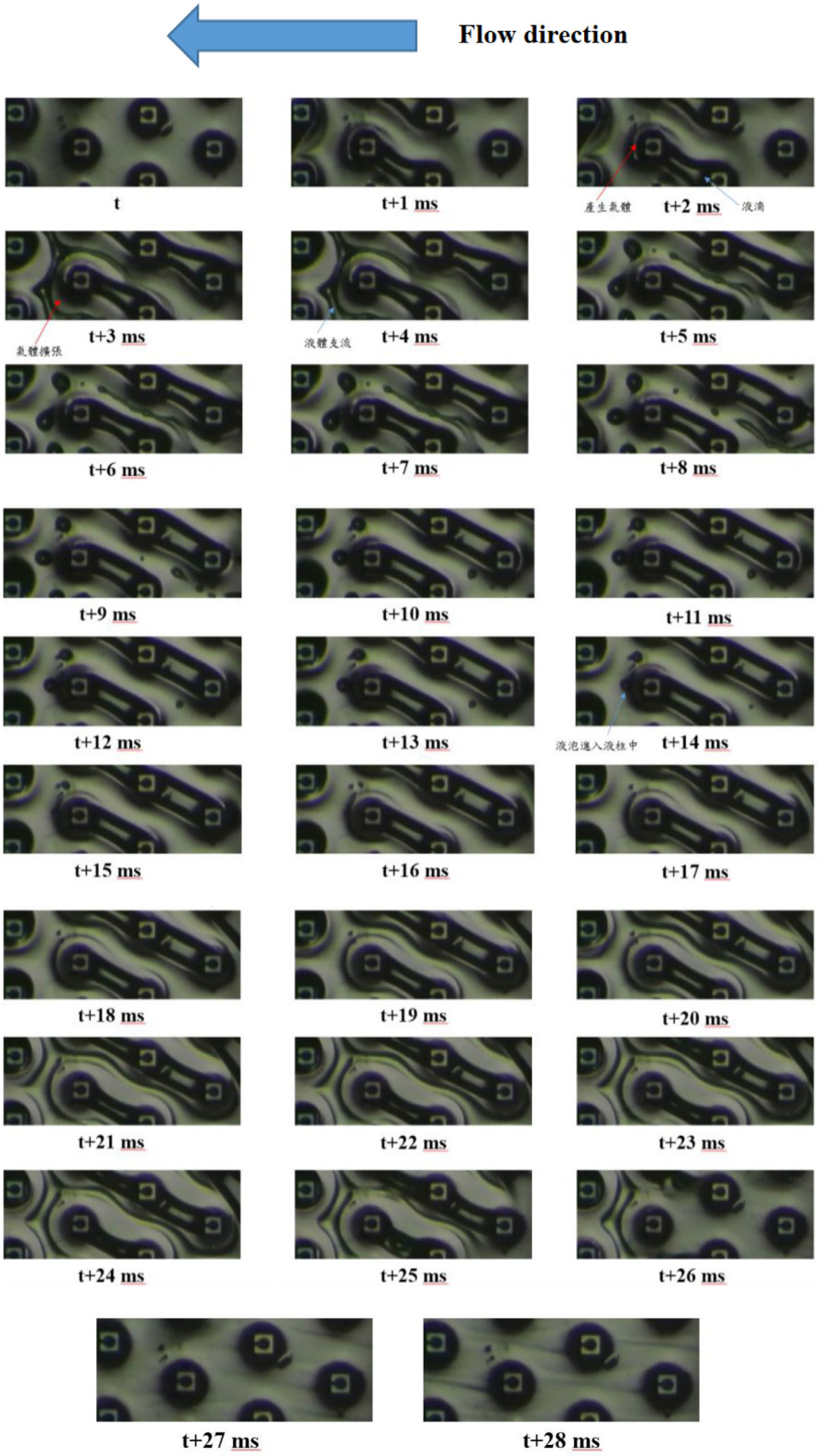

Fig. 18. Spectrum diagram of flow boiling for the case of C-60-15 and mass flux of $G = 137$ kg/m^{2}s when $q'' = 4.66$ W/cm^2 boiling.

5. Conclusion

In this study, the numerical simulation and experimental measurement are carried out for the heat transfer behavior of a microgap with an enhanced micro pin-fin surface. The main research outcomes can be summarized as follows:

1. The numerical simulation of this study and the experimental results of the heat transfer coefficient are compared with each other. The trend of the results was in good agreement, and the highest difference between the numerical results and the experimental results was at the low flow rates, and the error decreases by the increase of flow rate.
2. According to the numerical simulation, the reduction of the pore opening from 45 μm to 15 μm has no obvious influence on the single-phase heat transfer performance. The experimental data for the single-phase flow regime demonstrates that the opening pore shrinkage can indeed effectively reduce the pressure drop across the microgap with minimal effect on the heat transfer.
3. Shrinkage of the pore openings does reduce the degree of the surface-superheat required for boiling for high mass fluxes. The reason is that the surface of a pore with a smaller opening induces a negative pressure region at the downstream of the fin (in the pore). The internal negative pressure region with a small pore opening is more obvious at a high flow rate based on the numerical simulations of a single-phase flow. The temperature inside a pin fin with a smaller opening is higher. This phenomenon eases the bubble formation helps the flow to boil, and as a result, the boiling occurs at a comparatively lower temperature (lower surface supper heat temperature).
4. Experimental observations show that C-60-15 will be unstable when the single-phase flow regime transforms into the two phases regime. It is presumed that the bubbles are not stable in the pores. Therefore, when the bubble flows out of the pore, and the liquid is replenished, the flow is unstable near the air hole, which results in some degrees of temperature fluctuations at the test surface.
5. According to the experimental flow field observation, it is known that the nucleation pores can effectively generate bubbles after the liquid flows into the pores. This study establishes a two-phase flow field pattern in which the fins are staggered during initial boiling in the microchannel.

The present outcomes demonstrate that the opening and change in the geometry of the columnar micro pin-fins can change the onset of boiling heat transfer and the pressure drop. Hence, design of new pin-fin geometries and analysis of the effect of pin-fin geometrical structures on heat transfer behavior and pressure drop of the microgap can be addressed in future works. Moreover, the change in the saturation temperature of FC-72 was influenced by the onset of boiling and the surface-superheat temperatures. Therefore, analysis of the effect of various working fluids on the boiling heat transfer performance of micro gap heatsinks can be another direction of future studies.

Declaration of Competing Interest

None.

Acknowledgments

The authors acknowledge the financial support by the “Research Center of Energy Conservation for New Generation of Residential, Commercial, and Industrial Sectors” from The Featured Areas Research Center Program within the framework of the Higher Education Sprout Project by the Ministry of Education (MOE) in Taiwan.

References

[1] C. Woodcock, X. Yu, J. Plawsky, Y. Peles, Piranha Pin Fin (PPF)—Advanced flow boiling microstructures with low surface tension dielectric fluids, Int. J. Heat Mass Transf. 90 (2015) 591–604.
[2] A. Kosar, Y. Peles, TCPT-2006-096. R2: micro scale pin fin heat sinks—Parametric performance evaluation study, IEEE Trans. Compon. Packag. Technol. 30 (4) (2007) 855–865.
[3] Y. Wang, J.-H. Shin, C. Woodcock, X. Yu, Y. Peles, Experimental and numerical study about local heat transfer in a microchannel with a pin fin, Int. J. Heat Mass Transf. 121 (2018) 534–546.
[4] D. Kong, K.W. Jung, S. Jung, D. Jung, J. Schaadt, M. Iyengar, C. Malone, C.R. Kharangate, M. Asheghi, K.E. Goodson, Single-phase thermal and hydraulic performance of embedded silicon micro-pin fin heat sinks using R245fa, Int. J. Heat Mass Transf. 141 (2019) 145–155.
[5] Y. Xiangfei, C. Woodcock, Y. Peles, J. Plawsky, Single-phase modeling in microchannel with Piranha Pin Fin, (2015).
[6] W. Li, F. Yang, T. Alam, X. Qu, B. Peng, J. Khan, C. Li, Enhanced flow boiling in microchannels using auxiliary channels and multiple micronozzles (I): characterizations of flow boiling heat transfer, Int. J. Heat Mass Transf. 116 (2018) 208–217.
[7] W. Li, J. Ma, T. Alam, F. Yang, J. Khan, C. Li, Flow boiling of HFE-7100 in silicon microchannels integrated with multiple micro-nozzles and reentry micro-cavities, Int. J. Heat Mass Transf. 123 (2018) 354–366.
[8] T. Bevis, B. Burk, J. Hoke, J. Kotovsky, J. Hamilton, T. Bandhauer, Flow boiling of R134a in a high surface area microchannel array for high-flux laser diode cooling, Heat Transf. Res. (2018).
[9] D. Ma, G. Xia, L. Zong, Y. Jia, Y. Tang, R. Zhi, Experimental investigation of flow boiling heat transfer performance in zigzag microchannel heat sink for electronic cooling devices, Int. J. Therm. Sci. 145 (2019) 106003.
[10] W. Li, Y. Lin, K. Zhou, J. Li, J. Zhu, Local heat transfer of saturated flow boiling in vertical narrow microchannel, Int. J. Therm. Sci. 145 (2019) 105996.
[11] F.J. do Nascimento, T.A. Moreira, G. Ribatski, Flow boiling critical heat flux of DI-water and nanofluids inside smooth and nanoporous round microchannels, Int. J. Heat Mass Transf. 139 (2019) 240–253.
[12] C. Huh, M.H. Kim, Pressure drop, boiling heat transfer and flow patterns during flow boiling in a single microchannel, Heat Transf. Eng. 28 (8–9) (2007) 730–737.
[13] S.-S. Hsieh, C.-Y. Lin, Subcooled convective boiling in structured surface microchannels, J. Micromech. Microeng. 20 (1) (2009) 015027.
[14] J. Mathew, P.-S. Lee, T. Wu, C.R. Yap, Experimental study of flow boiling in a hybrid microchannel-microgap heat sink, Int. J. Heat Mass Transf. 135 (2019) 1167–1191.
[15] P. Asrar, X. Zhang, C.E. Green, M. Bakir, Y.K. Joshi, Flow boiling of R245fa in a microgap with staggered circular cylindrical pin fins, Int. J. Heat Mass Transf. 121 (2018) 329–342.
[16] D. Deng, L. Chen, W. Wan, T. Fu, X. Huang, Flow boiling performance in pin fin-interconnected reentrant microchannels heat sink in different operational conditions, Appl. Therm. Eng. 150 (2019) 1260–1272.
[17] Y. Lie, J. Ke, W. Chang, T. Cheng, T. Lin, Saturated flow boiling heat transfer and associated bubble characteristics of FC-72 on a heated micro-pin-finned silicon chip, Int. J. Heat Mass Transf. 50 (19–20) (2007) 3862–3876.
[18] C.-J. Kuo, Y. Peles, Flow boiling of coolant (HFE-7000) inside structured and plain wall microchannels, J. Heat Transf. 131 (12) (2009) 121011.
[19] A. Koşar, Y. Peles, Boiling heat transfer in a hydrofoil-based micro pin fin heat sink, Int. J. Heat Mass Transf. 50 (5–6) (2007) 1018–1034.
[20] S. Krishnamurthy, Y. Peles, Flow boiling of water in a circular staggered micro-pin fin heat sink, Int. J. Heat Mass Transf. 51 (5–6) (2008) 1349–1364.
[21] C. Falsetti, H. Jafarpoorchekab, M. Magnini, N. Borhani, J. Thome, Two-phase operational maps, pressure drop, and heat transfer for flow boiling of R236fa in a micro-pin fin evaporator, Int. J. Heat Mass Transf. 107 (2017) 805–819.
[22] W. Qu, A. Siu-Ho, Experimental study of saturated flow boiling heat transfer in an array of staggered micro-pin-fins, Int. J. Heat Mass Transf. 52 (7–8) (2009) 1853–1863.
[23] A. Ma, J. Wei, M. Yuan, J. Fang, Enhanced flow boiling heat transfer of FC-72 on micro-pin-finned surfaces, Int. J. Heat Mass Transf. 52 (13–14) (2009) 2925–2931.
[24] W. Wan, D. Deng, Q. Huang, T. Zeng, Y. Huang, Experimental study and optimization of pin fin shapes in flow boiling of micro pin fin heat sinks, Appl. Therm. Eng. 114 (2017) 436–449.
[25] M. Law, P.-S. Lee, A comparative study of experimental flow boiling heat transfer and pressure characteristics in straight-and oblique-finned microchannels, Int. J. Heat Mass Transf. 85 (2015) 797–810.
[26] C. Woodcock, C. Ng'oma, M. Sweet, Y. Wang, Y. Peles, J. Plawsky, Ultra-high heat flux dissipation with Piranha Pin Fins, Int. J. Heat Mass Transf. 128 (2019) 504–515.
[27] X. Yu, C. Woodcock, Y. Wang, J. Plawsky, Y. Peles, A comparative study of flow boiling in a microchannel with Piranha Pin Fins, J. Heat Transf. 138 (11) (2016) 111502.
[28] X. Yu, C. Woodcock, Y. Wang, J. Plawsky, Y. Peles, Enhanced subcooled flow boiling heat transfer in microchannel with Piranha Pin Fin, J. Heat Transf. 139 (11) (2017) 112402.
[29] W.-R. Liao, L.-H. Chien, M. Ghalambaz, W.-M. Yan, Experimental study of boiling heat transfer in a microchannel with nucleated-shape columnar micro-pin-fins, Int. Commun. Heat Mass Transf. 108 (2019) 104277.

[30] L.-H. Chien, W.-R. Liao, M. Ghalambaz, W.-M. Yan, Experimental study on convective boiling of micro-pin-finned channels with parallel arrangement fins for FC-72 dielectric fluid, Int. J. Heat Mass Transf. 138 (2019) 390–400.
[31] L.-H. Chien, W.-R. Liao, M. Ghalambaz, W.-M. Yan, Experimental study on convective boiling flow and heat transfer in a microgap enhanced with a staggered arrangement of nucleated micro-pin-fins, Int. J. Heat Mass Transf. 144 (2019) 118653.
[32] V.P. Carey, Liquid Vapor Phase Change phenomena: an Introduction to the Thermophysics of Vaporization and Condensation Processes in Heat Transfer Equipment, CRC Press, 1992.
[33] V.P. Carey, Liquid-Vapor Phase-change Phenomena, CRC Press, 1992.